The Astrophysical Journal, 789:146 (8pp), 2014 July 10 doi:10.1088/0004-637X/789/2/146

SYNCHROTRON SELF-INVERSE COMPTON RADIATION FROM REVERSE SHOCK ON GRB 120326A

Yuji Urata[1], Kuiyun Huang[2,3], Satoko Takahashi[2,4,5], Myungshin Im[6], Kazutaka Yamaoka[7,8], Makoto Tashiro[9], Jae-Woo Kim[6], Minsung Jang[6], and Soojong Pak[10]
[1] Institute of Astronomy, National Central University, Chung-Li 32054, Taiwan; urata@astro.ncu.edu.tw
[2] Academia Sinica Institute of Astronomy and Astrophysics, Taipei 106, Taiwan
[3] Department of Mathematics and Science, National Taiwan Normal University, Lin-kou District, New Taipei City 24449, Taiwan
[4] Joint ALMA Observatory, Alonso de Cordova 3108, Vitacura, Santiago, Chile
[5] National Astronomical Observatory of Japan, 2-21-1 Osawa, Mitaka, Tokyo 181-8588, Japan
[6] Center for the Exploration of the Origin of the Universe, Department of Physics and Astronomy, FPRD, Seoul National University, Shillim-dong, San 56-1, Kwanak-gu, Seoul, Korea
[7] Solar-Terrestrial Environment Laboratory, Nagoya University, Furo-cho, Chikusa-ku, Nagoya, Aichi 464-8601, Japan
[8] Division of Particle and Astrophysical Science, Graduate School of Science, Nagoya University, Furo-cho, Chikusa-ku, Nagoya, Aichi 464-8601, Japan
[9] Department of Physics, Saitama University, Shimo-Okubo, Saitama 338-8570, Japan
[10] School of Space Research, Kyung Hee University, Yongin, Gyeonggi 446-701, Korea
Received 2013 November 27; accepted 2014 May 14; published 2014 June 24

ABSTRACT

We present multi-wavelength observations of a typical long duration GRB 120326A at $z = 1.798$, including rapid observations using a Submillimeter Array (SMA) and a comprehensive monitoring in the X-ray and optical. The SMA observation provided the fastest detection to date among seven submillimeter afterglows at 230 GHz. The prompt spectral analysis, using *Swift* and *Suzaku*, yielded a spectral peak energy of $E_{\rm peak}^{\rm src} = 107.8^{+15.3}_{-15.3}$ keV and an equivalent isotropic energy of $E_{\rm iso}$ as $3.18^{+0.40}_{-0.32} \times 10^{52}$ erg. The temporal evolution and spectral properties in the optical were consistent with the standard forward shock synchrotron with jet collimation ($6.^{\circ}69 \pm 0.^{\circ}16$). The forward shock modeling, using a two-dimensional relativistic hydrodynamic jet simulation, was also determined by the reasonable burst explosion and the synchrotron radiation parameters for the optical afterglow. The X-ray light curve showed no apparent jet break and the temporal decay index relation between the X-ray and optical ($\alpha o - \alpha_X = -1.45 \pm 0.10$) indicated different radiation processes in each of them. Introducing synchrotron self-inverse Compton radiation from reverse shock is a possible solution, and the detection and slow decay of the afterglow in submillimeter supports that this is a plausible idea. The observed temporal evolution and spectral properties, as well as forward shock modeling parameters, enabled us to determine reasonable functions to describe the afterglow properties. Because half of the events share similar properties in the X-ray and optical as the current event, GRB 120326A will be a benchmark with further rapid follow-ups, using submillimeter instruments such as an SMA and the Atacama Large Millimeter/submillimeter Array.

Key words: gamma-ray burst: individual (120326a) – radiation mechanisms: non-thermal

Online-only material: color figures

1. INTRODUCTION

Gamma-ray bursts (GRBs) are among the most powerful explosions in the universe and are observationally characterized by intense short flashes primarily in a high-energy band (so-called prompt emission) and long-lived afterglows observed from X-ray to radio wavelengths. The GRB afterglow is believed to involve a relativistically expanding fireball (e.g., Meszaros & Rees 1997). Interstellar matter (ISM) influences the fireball shell after it has been collected and considerable energy is transferred from the shell to the ISM. The energy transfer is caused by two shocks: a forward shock propagating into the ISM and a reverse shock propagating into the shell. It is also believed that the forward shock produces long-lived afterglows and the reverse shock generates short-lived bright optical flashes (e.g., Akerlof et al. 1999) and/or intense radio afterglows (e.g., Kulkarni et al. 1999).

A number of afterglows have been densely monitored in X-ray and optical bands since the launch of the *Swift* satellite (Gehrels et al. 2004), and a significant number of afterglows showed the different temporal evolutions in X-ray and optical bands. These results indicated that the simple forward shock model cannot explain their behavior altogether and additional processes are required (e.g., Panaitescu et al. 2006; Huang et al. 2007; Urata et al. 2007; Li et al. 2012). Inverse Compton scattering and/or reverse shocks may play an important role in solving the problem. Panaitescu & Vestrand (2011) suggested local inverse Compton scattering to describe the X-ray band's faster decay compared with that of the optical. Kobayashi et al. (2007) introduced a synchrotron self-inverse Compton radiation from a reverse shock to explain the X-ray flare and its early afterglows. Thus, confirming the existence of reverse shocks at particularly longer wavelengths and ascertaining their typical occurrence conditions is critical. Because the expected lifetime of reverse shocks at longer wavelengths is substantially longer than the lifetime of those at optical wavelengths, decoding radiations into forward and reverse shock components is possible. In addition, numerous rapid optical follow-ups are missing the reverse shock components; however, several successful detections at optical wavelengths have been made.

The possible reason for the missing reverse shock component could be that the typical reverse shock synchrotron frequency is far below the optical band. Submillimeter observations are the key elements used to catch reverse shock and to understand the emission mechanism of GRB afterglows. Searching for reverse shock emission in the submillimeter wavelength would test this possibility. These submillimeter observations also provide clean measurements of source intensity, unaffected

by scintillation and extinction. However, no systematic submillimeter observational studies in the early afterglow phase exist. This has remained the case in reverse shock studies for some time. One of the main reasons for this is the absence of dedicated submillimeter telescopes and strategic follow-ups with rapid response which involve employing open-use telescopes for these challenging observations. In addition, it is nearly impossible to have rapid (several hours after the burst) follow-ups with current open-use telescopes which require manual preparation of the observational scripts. In addition to this technical problem, the sensitivities of current submillimeter telescopes, except for the Atacama Large Millimeter/submillimeter Array (ALMA), are not good enough to detect the number of afterglows in the submillimeter band (e.g., de Ugarte Postigo et al. 2012). Hence, rapid careful target selections are required to conduct effective submillimeter follow-up observations using open-use resources.

GRB 120326A was detected and localized using *Swift* (Siegel et al. 2012). The *Suzaku*/Wide-band All-Sky Monitor (*Suzaku*/WAM) and the *Fermi* Gamma-ray Burst Monitor (*Fermi*/GBM) also detected this burst, and quick-look spectral analyses were reported (Iwakiri et al. 2012; Collazzi 2012). The optical afterglow was discovered by Klotz et al. (2012) and observed at the early stage by using several telescopes. The optical afterglow also exhibited remarkable rebrightening (Walker et al. 2012). The afterglow at submillimeter and radio bands was also detected using an Submillimeter Array (SMA; Urata et al. 2012), the Combined Array for Research in Millimeter-wave Astronomy (Perley et al. 2012), and the Expanded Very Large Array (Laskar et al. 2012). The SMA observation provided the fastest afterglow detection (about 4.6×10^4 s after the burst) among seven submillimeter afterglows at 230 GHz, which are mostly detected about 1×10^5 s ($\sim$1 day) after the bursts. Although numerous follow-ups in various wavelengths have been conducted, submillimeter afterglow monitoring from the earlier phase ($<1 \times 10^5$ s) is still rare and essential to understand the puzzle of afterglow radiation. The redshift was determined to be $z = 1.798$, according to a series of metal absorption features (Tello et al. 2012). We used $f(t, \nu) \propto t^{\alpha}\nu^{\beta}$ to express the afterglow properties.

2. OBSERVATIONS

The *Swift* Burst Alert Telescope (*Swift*/BAT) triggered and located GRB 120326A at 01:20:29 (T_0) UT on 2012 March 26. *Swift* immediately slewed to the burst and the X-Ray Telescope (XRT) initiated follow-up observations at 59.5 s after the burst. The X-ray afterglow was identified and localized at R.A. = $18^{\rm h}15^{\rm m}36\overset{\rm s}{.}47$, decl. = $+69^{\circ}15'37\overset{''}{.}0$, with an uncertainty of $4\overset{''}{.}1$. The X-ray afterglow was observed using the XRT until $\sim 5 \times 10^5$ s. UVOT also obtained images by using the White filter starting 67 s after the burst and no counterpart in the band was observed.

The *Suzaku*/WAM also triggered the burst at 01:20:31.9 (T_0 + 2.9 s) UT on 2012 March 26. The WAM (Yamaoka et al. 2009) is a lateral shield of the Hard X-ray Detector (Takahashi et al. 2007) on board the *Suzaku* satellite (Mitsuda et al. 2007) and is a powerful GRB spectrometer covering an energy range of 50–5000 keV to determine prompt spectral energy peaks, $E_{\rm peak}$ (e.g., Ohno et al. 2008; Tashiro et al. 2007; Urata et al. 2009). As shown in Figure 1, the prompt X-ray and γ-ray light curves observed using the *Swift*/BAT and *Suzaku*/WAM exhibited a single fast rise and exponential decay structure.

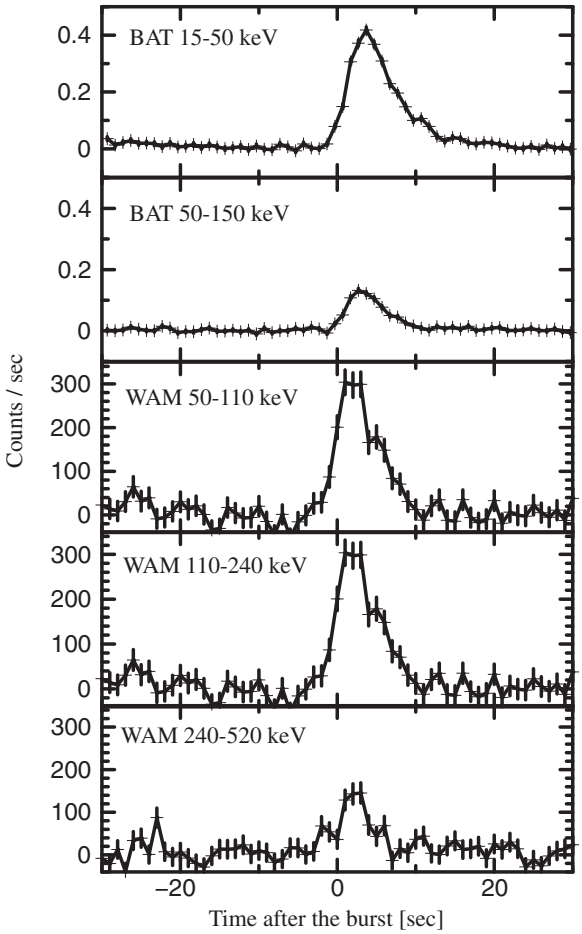

Figure 1. Prompt γ-ray light curves observed by *Swift*/BAT and *Suzaku*/WAM. The trigger time of *Swift*/BAT is used as T_0.

We performed the optical afterglow observations using the Lulin 1 m telescope (LOT; Huang et al. 2005) and the LOAO robotic 1 m telescope (Han et al. 2005; Lee et al. 2010) within the framework of the EAFON (Urata et al. 2003). Four color observations were made with LOT on the night of March 26. The LOAO data were obtained in the *R*-band filter from 2013 March 26 to April 2. The afterglow was also observed with Camera for Quasars in the Early Universe (Park et al. 2012; Kim et al. 2011; Lim et al. 2013) on the 2.1 m Otto-Struve Telescope of the McDonald observatory, Texas, USA. The data were obtained in g, r, i, z, and Y filters, starting at 2013 March 26, 10:09:22 (UT) and continued until April 2. The logs for both observations are summarized in Table 1.

We also triggered the submillimeter continuum follow-up observations by using the seven 6 m antennas of SMA (Ho et al. 2004). The first continuum observation at 230 GHz (with an 8 GHz bandwidth) was conducted at 10:15:05 on 2012 March 26, about 4.6×10^4 s after the BAT trigger. As Urata et al. (2012) reported, the submillimeter counterpart was observed at the location of the X-ray and optical afterglow. The continuous monitoring using the SMA was also performed at the same frequency setting on March 27, 29, 31, and April 6 and 11. Table 2 summarizes the scientific observations that were conducted for four nights, because of weather conditions and antenna reconfiguration. Figure 2 shows submillimeter light curves of all the GRB afterglows detected at the 230 GHz to date. Among all seven events, we successfully detected the earliest submillimeter afterglow on GRB 120326A. A possible

Table 1
Log of Optical Observations

Instruments	$T-T_0$ (s)	Filter	Exposure (s)	Flux Density (mJy)
CQUEAN	35818	*g*	120	$(5.031 \pm 1.114) \times 10^{-2}$
CQUEAN	36428	*g*	120	$(5.843 \pm 0.364) \times 10^{-2}$
LOT	62495	*g*	300	$(2.751 \pm 0.130) \times 10^{-2}$
LOT	66550	*g*	300	$(2.781 \pm 0.132) \times 10^{-2}$
CQUEAN	118878	*g*	120	$(1.549 \pm 0.072) \times 10^{-2}$
CQUEAN	203667	*g*	120	$(9.670 \pm 1.290) \times 10^{-3}$
CQUEAN	203788	*g*	120	$(7.200 \pm 1.310) \times 10^{-3}$
CQUEAN	203909	*g*	120	$(9.820 \pm 1.150) \times 10^{-3}$
CQUEAN	210775	*g*	120	$(8.840 \pm 2.050) \times 10^{-3}$
CQUEAN	210896	*g*	120	$(9.580 \pm 2.540) \times 10^{-3}$
CQUEAN	211018	*g*	120	$(1.460 \pm 0.271) \times 10^{-2}$
CQUEAN	291923	*g*	120 × 5	$(5.800 \pm 1.330) \times 10^{-3}$
CQUEAN	382503	*g*	300 × 3	$(2.600 \pm 0.320) \times 10^{-3}$
CQUEAN	468068	*g*	300 × 3	$(1.550 \pm 0.420) \times 10^{-3}$
LOAO	119527	*R*	300	$(7.517 \pm 0.848) \times 10^{-2}$
LOAO	119845	*R*	300	$(6.792 \pm 0.654) \times 10^{-2}$
LOAO	120163	*R*	300	$(8.395 \pm 0.596) \times 10^{-2}$
LOAO	120532	*R*	300	$(1.019 \pm 0.055) \times 10^{-1}$
LOAO	120882	*R*	300	$(1.096 \pm 0.059) \times 10^{-1}$
LOAO	121197	*R*	300	$(8.395 \pm 0.596) \times 10^{-2}$
LOAO	206539	*R*	300	$(4.787 \pm 0.579) \times 10^{-2}$
LOAO	206865	*R*	300	$(4.365 \pm 0.633) \times 10^{-2}$
LOAO	207181	*R*	300	$(5.105 \pm 0.740) \times 10^{-2}$
LOAO	207498	*R*	300	$(3.565 \pm 0.373) \times 10^{-2}$
LOAO	301087	*R*	900	$(2.148 \pm 0.242) \times 10^{-2}$
LOAO	300315	*R*	900	$(2.128 \pm 0.275) \times 10^{-2}$
LOAO	303167	*R*	1200	$(2.884 \pm 0.349) \times 10^{-2}$
LOAO	589749	*R*	2700	$(5.750 \pm 0.880) \times 10^{-3}$
CQUEAN	31732	*r*	300	$(1.734 \pm 0.022) \times 10^{-1}$
CQUEAN	33129	*r*	300	$(1.636 \pm 0.008) \times 10^{-1}$
CQUEAN	34399	*r*	300	$(1.510 \pm 0.027) \times 10^{-1}$
CQUEAN	36739	*r*	300	$(1.478 \pm 0.010) \times 10^{-1}$
LOT	63503	*r*	300	$(8.434 \pm 0.177) \times 10^{-2}$
LOT	67564	*r*	300	$(8.591 \pm 0.165) \times 10^{-2}$
CQUEAN	117385	*r*	300	$(4.955 \pm 0.036) \times 10^{-2}$
CQUEAN	202218	*r*	120	$(1.812 \pm 0.207) \times 10^{-2}$
CQUEAN	202340	*r*	120	$(2.526 \pm 0.175) \times 10^{-2}$
CQUEAN	202461	*r*	120	$(2.544 \pm 0.141) \times 10^{-2}$
CQUEAN	209219	*r*	120	$(2.586 \pm 0.236) \times 10^{-2}$
CQUEAN	209633	*r*	120	$(2.720 \pm 0.116) \times 10^{-2}$
CQUEAN	209754	*r*	120	$(2.496 \pm 0.119) \times 10^{-2}$
CQUEAN	286528	*r*	120	$(1.715 \pm 0.075) \times 10^{-2}$
CQUEAN	286650	*r*	120	$(1.712 \pm 0.067) \times 10^{-2}$
CQUEAN	286771	*r*	120	$(1.603 \pm 0.065) \times 10^{-2}$
CQUEAN	295768	*r*	120	$(2.072 \pm 0.291) \times 10^{-2}$
CQUEAN	381506	*r*	180	$(8.050 \pm 0.380) \times 10^{-3}$
CQUEAN	381688	*r*	180	$(7.040 \pm 0.390) \times 10^{-3}$
CQUEAN	381869	*r*	180	$(8.500 \pm 0.380) \times 10^{-3}$
CQUEAN	466726	*r*	300	$(5.300 \pm 0.710) \times 10^{-3}$
CQUEAN	467028	*r*	300	$(3.770 \pm 0.670) \times 10^{-3}$
CQUEAN	467329	*r*	300	$(4.860 \pm 0.550) \times 10^{-3}$
CQUEAN	552707	*r*	300	$(2.890 \pm 0.270) \times 10^{-3}$
CQUEAN	553009	*r*	300	$(2.930 \pm 0.290) \times 10^{-3}$
CQUEAN	553310	*r*	300	$(3.070 \pm 0.300) \times 10^{-3}$
CQUEAN	639867	*r*	300 × 6	$(1.970 \pm 0.300) \times 10^{-3}$
CQUEAN	32074	*i*	300	$(3.621 \pm 0.010) \times 10^{-1}$
CQUEAN	33448	*i*	300	$(3.701 \pm 0.005) \times 10^{-1}$
CQUEAN	34711	*i*	300	$(3.803 \pm 0.023) \times 10^{-1}$
CQUEAN	37050	*i*	300	$(3.311 \pm 0.039) \times 10^{-1}$
LOT	68583	*i*	300	$(1.964 \pm 0.028) \times 10^{-1}$
LOT	64510	*i*	300	$(1.982 \pm 0.021) \times 10^{-1}$
CQUEAN	117705	*i*	300	$(1.257 \pm 0.003) \times 10^{-1}$
CQUEAN	202624	*i*	120	$(6.634 \pm 0.084) \times 10^{-2}$
CQUEAN	202746	*i*	120	$(6.164 \pm 0.082) \times 10^{-2}$
CQUEAN	202867	*i*	120	$(7.226 \pm 0.084) \times 10^{-2}$

Table 1
(Continued)

Instruments	$T-T_0$ (s)	Filter	Exposure (s)	Flux Density (mJy)
CQUEAN	209979	*i*	120	$(5.834 \pm 0.089) \times 10^{-2}$
CQUEAN	210100	*i*	120	$(6.346 \pm 0.102) \times 10^{-2}$
CQUEAN	210222	*i*	120	$(6.188 \pm 0.103) \times 10^{-2}$
CQUEAN	286927	*i*	120	$(4.194 \pm 0.069) \times 10^{-2}$
CQUEAN	287048	*i*	120	$(4.292 \pm 0.099) \times 10^{-2}$
CQUEAN	287169	*i*	120	$(4.360 \pm 0.071) \times 10^{-2}$
CQUEAN	287313	*i*	120	$(4.186 \pm 0.063) \times 10^{-2}$
CQUEAN	295903	*i*	120	$(4.150 \pm 0.235) \times 10^{-2}$
CQUEAN	296025	*i*	120	$(5.662 \pm 0.943) \times 10^{-2}$
CQUEAN	380844	*i*	180	$(2.118 \pm 0.036) \times 10^{-2}$
CQUEAN	381025	*i*	180	$(2.092 \pm 0.038) \times 10^{-2}$
CQUEAN	381206	*i*	180	$(2.278 \pm 0.036) \times 10^{-2}$
CQUEAN	465783	*i*	300	$(1.256 \pm 0.056) \times 10^{-2}$
CQUEAN	466084	*i*	300	$(1.178 \pm 0.060) \times 10^{-2}$
CQUEAN	466386	*i*	300	$(1.390 \pm 0.057) \times 10^{-2}$
CQUEAN	553652	*i*	300	$(7.760 \pm 0.280) \times 10^{-3}$
CQUEAN	553954	*i*	300	$(8.820 \pm 0.280) \times 10^{-3}$
CQUEAN	554255	*i*	300	$(8.200 \pm 0.270) \times 10^{-3}$
CQUEAN	648922	*i*	300 × 6	$(4.880 \pm 0.290) \times 10^{-3}$
CQUEAN	32416	*z*	300	$(9.325 \pm 0.016) \times 10^{-1}$
CQUEAN	33766	*z*	300	$(9.250 \pm 0.021) \times 10^{-1}$
CQUEAN	35023	*z*	300	$(9.018 \pm 0.073) \times 10^{-1}$
LOT	65534	*z*	300	$(5.278 \pm 0.088) \times 10^{-1}$
LOT	69604	*z*	300	$(4.358 \pm 0.085) \times 10^{-1}$
CQUEAN	118015	*z*	300	$(3.025 \pm 0.006) \times 10^{-1}$
CQUEAN	203042	*z*	120	$(1.639 \pm 0.020) \times 10^{-1}$
CQUEAN	203163	*z*	120	$(1.970 \pm 0.032) \times 10^{-1}$
CQUEAN	203285	*z*	120	$(1.660 \pm 0.024) \times 10^{-1}$
CQUEAN	210347	*z*	120	$(1.744 \pm 0.018) \times 10^{-1}$
CQUEAN	210468	*z*	120	$(1.650 \pm 0.018) \times 10^{-1}$
CQUEAN	210589	*z*	120	$(1.744 \pm 0.019) \times 10^{-1}$
CQUEAN	287478	*z*	120	$(1.113 \pm 0.017) \times 10^{-1}$
CQUEAN	287600	*z*	120	$(1.112 \pm 0.017) \times 10^{-1}$
CQUEAN	287721	*z*	120	$(1.147 \pm 0.016) \times 10^{-1}$
CQUEAN	380256	*z*	120	$(5.236 \pm 0.079) \times 10^{-2}$
CQUEAN	380438	*z*	120	$(5.696 \pm 0.083) \times 10^{-2}$
CQUEAN	380619	*z*	120	$(5.524 \pm 0.078) \times 10^{-2}$
CQUEAN	464838	*z*	180	$(2.944 \pm 0.141) \times 10^{-2}$
CQUEAN	465140	*z*	180	$(2.680 \pm 0.103) \times 10^{-2}$
CQUEAN	465441	*z*	180	$(2.204 \pm 0.100) \times 10^{-2}$
CQUEAN	554653	*z*	300	$(1.784 \pm 0.060) \times 10^{-2}$
CQUEAN	554955	*z*	300	$(2.248 \pm 0.062) \times 10^{-2}$
CQUEAN	555256	*z*	300	$(2.120 \pm 0.064) \times 10^{-2}$
CQUEAN	32776	*Y*	300	1.585 ± 0.004
CQUEAN	118338	*Y*	300	$(5.005 \pm 0.025) \times 10^{-1}$
CQUEAN	205445	*Y*	120 × 6	$(3.576 \pm 0.054) \times 10^{-1}$
CQUEAN	288007	*Y*	120 × 3	$(2.672 \pm 0.053) \times 10^{-1}$

reason for this successful submillimeter monitoring was the target selection using the quick optical follow-ups.

3. ANALYSIS AND RESULTS

The BAT data were analyzed using the standard BAT analysis software included in HEADAS version 6.12. The time-averaged spectrum (15–150 keV) from $T_0 - 2$ to $T_0 + 11$ s was extracted using `batgrbproduct`. Response matrices were generated by the task `batdrmgen`, using the latest spectral redistribution matrices. The WAM spectral and temporal data were extracted using `hxdmkwamlc` and `hxdmkwamspec` in HEADAS version 6.12. The background was estimated using the fitting model described in Sugita et al. (2009). Response matrices were

Table 2
Log of SMA Observations

Instruments	Observing Period (UT)	$T-T_0$ (s)	Band (GHz)	Beam Size	Flux Density (mJy)
SMA	2012 Mar 26 13:00–15:00	45571	230	$1''.74 \times 1''.14$	2.84 ± 0.86
SMA	2012 Mar 26 15:10–17:30	53971	230	$1''.69 \times 1''.02$	3.56 ± 0.75
SMA	2012 Mar 26 18:00–20:15	64171	230	$2''.03 \times 0''.96$	3.36 ± 1.04
SMA	2012 Mar 27 13:25–19:15	138480	230	$1''.62 \times 1''.11$	2.38 ± 0.51
SMA	2012 Mar 29 12:45–18:50	310290	230	$0''.62 \times 0''.37$	1.76 ± 0.50
SMA	2012 Apr 11 15:50–21:10	1377571	230	$0''.55 \times 0''.42$	$<1.44\,(3\sigma)$

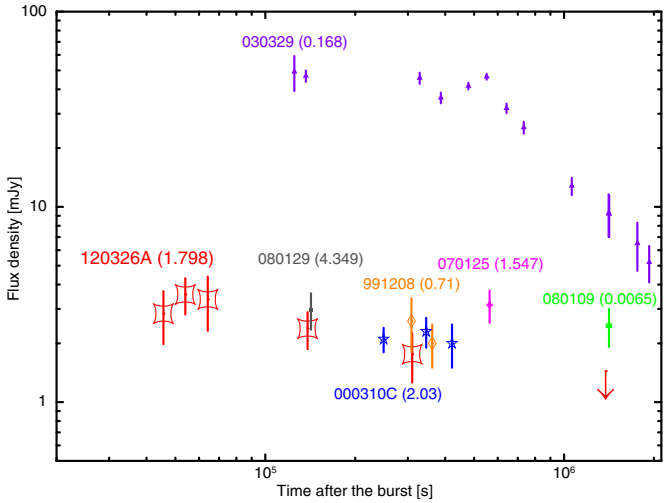

Figure 2. Light curves of all the submillimeter afterglows detected in the 230 GHz band to date. The SMA observation on GRB 120326A provides the earliest submillimeter detection and continuous monitoring. The values noted in brackets are the redshifts of each event. The samples are taken from Galama et al. (2000) for 991208, Berger et al. (2000) for 0000301C, Resmi et al. (2005) and Sheth et al. (2003) for 030329, Chandra et al. (2008) for 070125, Gorosabel et al. (2010) for 080109, and Greiner et al. (2009) for 080129.

(A color version of this figure is available in the online journal.)

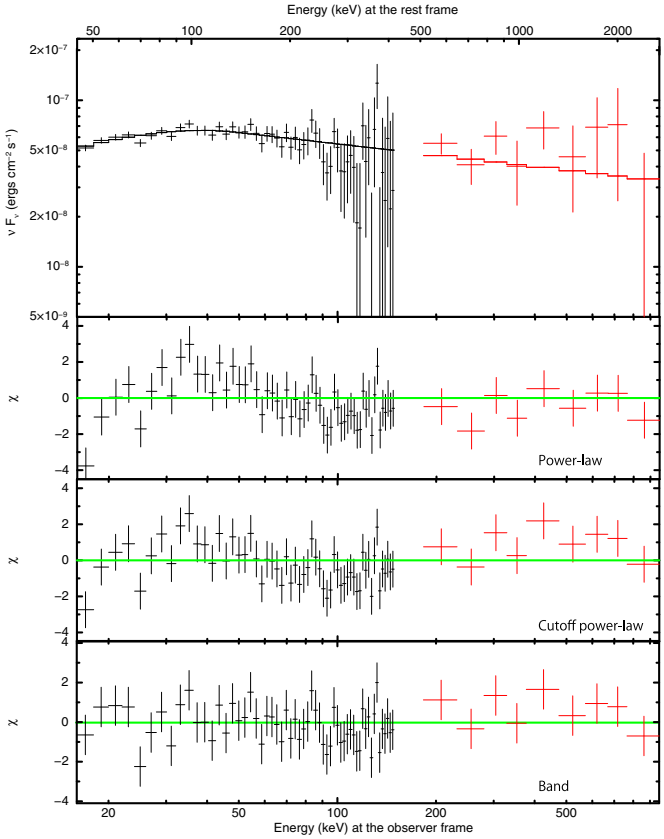

Figure 3. Time-averaged spectrum of the prompt emission, observed using *Swift*/BAT and *Suzaku*/WAM. The BAT and WAM data are shown in black and red, respectively. In the top panel, the solid lines indicate the best-fit Band function model. The lower panels show residuals for fitting with power law (second), power law with exponential cutoff (third), and Band (fourth) models.

(A color version of this figure is available in the online journal.)

generated by the WAM response generator as described in Ohno et al. (2008). We used three models for the joint spectral fitting: the power-law model, power law with exponential cutoff model, and the Band function model. As shown in Figure 3, the spectrum was reasonably fitted with the Band function. The fitting yielded a low-energy photon index of $1.17^{+0.53}_{-0.32}$, a high-energy photon index of $2.23^{+0.09}_{-0.11}$, and a $\nu F\nu$ spectrum peak energy in the source frame $E^{\rm src}_{\rm peak}$ of $107.8^{+15.2}_{-15.3}$ keV ($\chi^2/\nu = 0.92$ for $\nu = 63$). Both the power law ($\chi^2/\nu = 1.55$ for $\nu = 65$) and power law with exponential cutoff models ($\chi^2/\nu = 1.38$ for $\nu = 67$) were not acceptable, leaving the curvature of the residuals around 30–40 keV at the observer frame (the second and third panels in Figure 3). We also estimated the equivalent isotropic radiated energy in the prompt phase at the 1–10,000 keV band $E_{\rm iso}$ as $3.18^{+0.40}_{-0.32} \times 10^{52}$ erg, assuming cosmological parameters: $H_0 = 71$ km s^{-1} Mpc^{-1}, $\Omega_m = 0.27$, and $\Omega_\Lambda = 0.73$.

We obtained a reduced *Swift*/XRT light curve with a flux density unit at 10 keV from the U.K. Swift Science Data Center (Evans et al. 2007, 2009). The light curves shown in Figure 4 were suitably fitted using the broken power-law model described in Urata et al. (2009), using the best-fitted parameters of $\alpha_{X1} = 0.19 \pm 0.09$, $\alpha_{X2} = -2.35 \pm 0.15$, and $t_{bX} = (5.29 \pm 0.32) \times 10^4$ s. We also generated the time-averaged spectrum at a mean time of 6.47×10^4 s (from 55741 to 73639 s). The spectra were suitably fitted using the power law modified by photo-electric absorptions (Galactic and intrinsic), and the photon index was estimated as $1.95^{+0.18}_{-0.17}$.

A standard routine, including bias subtraction and flat-fielding corrections, was employed to processes the optical data by using the IRAF package. The DAOPHOT package was used to perform the aperture photometry of the GRB images. Standard star observation in one night is used to derive magnitudes of reference stars in the vicinity of the GRB afterglow, and these reference stars were used to perform photometry of the afterglow. We also made use of the Pan-STARRS1 3π catalogs (Magnier et al. 2013; Schlafly et al. 2012; Tonry et al. 2012) to calibrate our g'-, r'-, i'-, z'-, and Y-band data. As shown in Figure 4, the light curves in the g', r', i', and z' bands

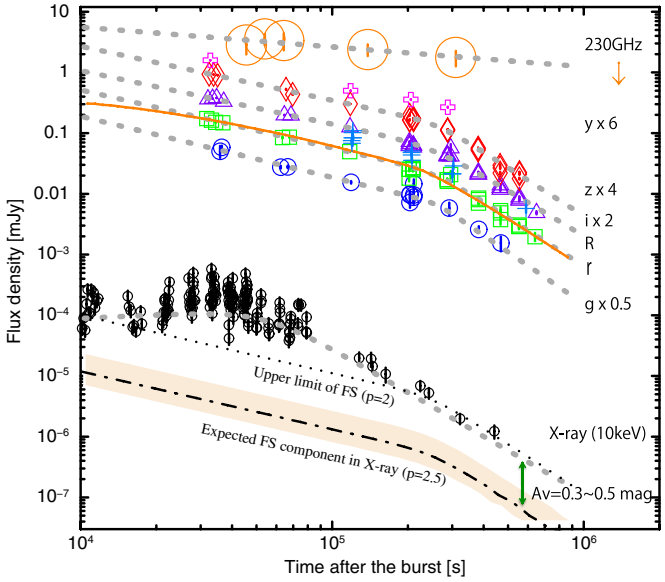

Figure 4. X-ray, optical, and submillimeter light curves of the GRB 120326A afterglow. The gray dotted lines show the best analytical fitted functions described in the text. The orange solid line shows the best modeling function for the *r*-band light curve obtained with the numerical simulation using boxfit. The black dashed-dotted and dotted lines indicate the shifted optical light curve to the X-ray bands by a factor of $(\nu_X/\nu_{\rm opt})^{-p/2}$ with $p = 2.5$ and $p = 2$, respectively.

(A color version of this figure is available in the online journal.)

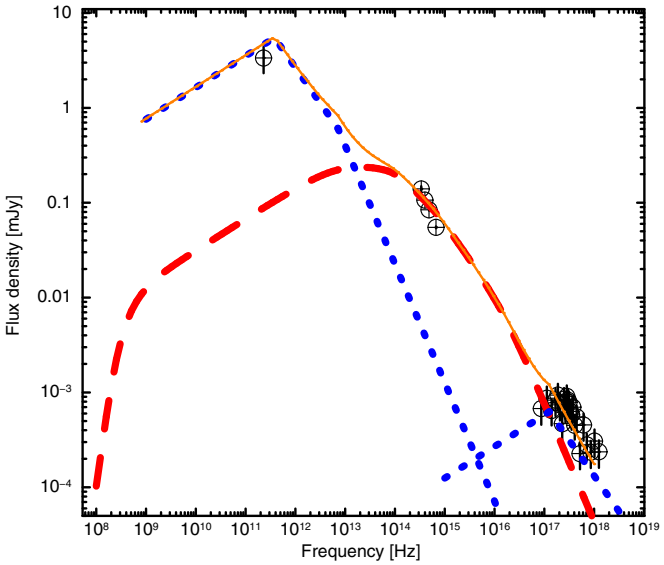

Figure 5. Spectral energy distribution at 6.42×10^4 s after the burst. The red dashed line shows the forward shock synchrotron model spectrum calculated using the boxfit code with the same parameters for the best modeling light curve shown in Figure 4. The blue dotted lines show the reverse shock synchrotron radiation and its self-inverse Compton component calculated based on Kobayashi et al. (2007) using the observed values and model function for the forward shock component.

(A color version of this figure is available in the online journal.)

indicated the achromatic temporal break at $\sim 2.6 \times 10^5$ s. We successfully fitted the broken power-law model to the g'-, r'-, i'-, and z'-band light curves. Regarding the g' band, we have obtained $\alpha_{g1} = -1.01 \pm 0.06$, $\alpha_{g2} = -2.84 \pm 0.16$, and $t_{bg} = (2.58 \pm 0.15) \times 10^5$ s; regarding the r' band, $\alpha_{r1} = -0.96 \pm 0.01$, $\alpha_{r2} = -2.64 \pm 0.09$, and $t_{br} = (2.58 \pm 0.07) \times 10^5$ s; regarding the i' band, $\alpha_{i1} = -0.88 \pm 0.02$, $\alpha_{i2} = -2.48 \pm 0.05$, and $t_{bi} = (2.51 \pm 0.10) \times 10^5$ s; regarding the z' band, $\alpha_{z1} = -0.89 \pm 0.01$, $\alpha_{z2} = -2.64 \pm 0.10$, and $t_{bz} = (2.63 \pm 0.06) \times 10^5$ s; and regarding the y' band, we fitted the light curve by using the simple power-law model, because the y'-band observations covered only before the temporal break. The light curve was fitted with the model and we obtained $\alpha_y = -0.87 \pm 0.03$. The decay indices before and after the break are ~ -1 and ~ -2, respectively, which is highly consistent with typical well-observed long GRB optical afterglows. In Figure 5, we plot the spectral flux distribution with the submillimeter and X-ray data. We fitted the optical data alone using a power-law function and obtained $\beta = -1.44 \pm 0.10$, -1.11 ± 0.09, and -1.18 ± 0.17 at $t = 6.42 \times 10^4$ s, 1.38×10^5 s, and 3.10×10^5 s, respectively. To remove the effects of the Galactic interstellar extinction, we used the reddening map by Schlafly & Finkbeiner (2011).

The raw data of the SMA observations were calibrated using the MIR and MIRIAD packages and images were made with the natural weighting. Regarding the first night of observation, we split the data into three periods to describe the temporal evolution of submillimeter afterglow. Table 2 summarizes each observation period and flux density measurements (upper part). Because of adverse weather conditions during the first 1.08×10^4 s, only the data recorded after 13:00 on March 26 UT were used for the scientific analysis. In the final period, we constrained the 3σ upper limit. With our SMA follow-ups, we successfully monitored the afterglow from 4.32×10^4 to 3.46×10^5 s as shown in Figure 4. The submillimeter afterglow exhibited a flat evolution with slight brightening between the first and second periods. To describe the temporal evolution, we fitted the submillimeter data with the single power-law function and obtained $\alpha_{\rm submillimeter} = -0.33 \pm 0.08$, which was considerably flatter than those of the X-ray and optical.

4. DISCUSSION

4.1. Prompt Emission and Energetics Relations

The joint fitting of the *Swift*/BAT and *Suzaku*/WAM suitably constrained the spectral parameters of the prompt emission of GRB 120326A that are critical to characterize the event. As shown in Figure 6, the spectral peak energy in the source frame, $E^{\rm src}_{\rm peak}$, is one of the lowest events among the sample of the joint *Swift*/BAT–*Suzaku*/WAM analysis. The trend is similar to that of the $\nu F\nu$ spectral peak energy at the observer frame $E^{\rm obs}_{\rm peak}$ in comparison to a larger set of $E^{\rm obs}_{\rm peak}$ values of 479 GRBs drawn from the *Fermi*/GBM catalog (von Kienlin et al. 2014); however, the *Fermi*/GBM measurements do not represent $E^{\rm src}_{\rm peak}$ due to the lack of redshift information. By comparing with the *HETE-2* sample (Sakamoto et al. 2005), GRB 120326A can be categorized as X-ray-rich GRBs. Using the definition with *Swift*/BAT data (Sakamoto et al. 2008), we confirm that GRB 120326A with an $\sim$0.74 fluence ratio in the 25–50 keV and 50–100 keV bands falls into the X-ray-rich GRB family.

The abundance of the multi-color optical light curves for estimating the jet break time suggests that GRB 120326A is a favorable target for evaluating $E^{\rm src}_{\rm peak}$–$E_{\rm iso}$ (Amati et al. 2002) and $E^{\rm src}_{\rm peak}$–E_γ (Ghirlanda et al. 2007) relations. Here, $E^{\rm src}_{\rm peak}$–E_γ is the correlation between the intrinsic spectrum peak energy, $E^{\rm src}_{\rm peak}$, and the jet collimation-corrected energy in the prompt phase, E_γ. The closure relation of the observed optical temporal decay and the spectral indices (e.g., Sari et al. 1999; Zhang &

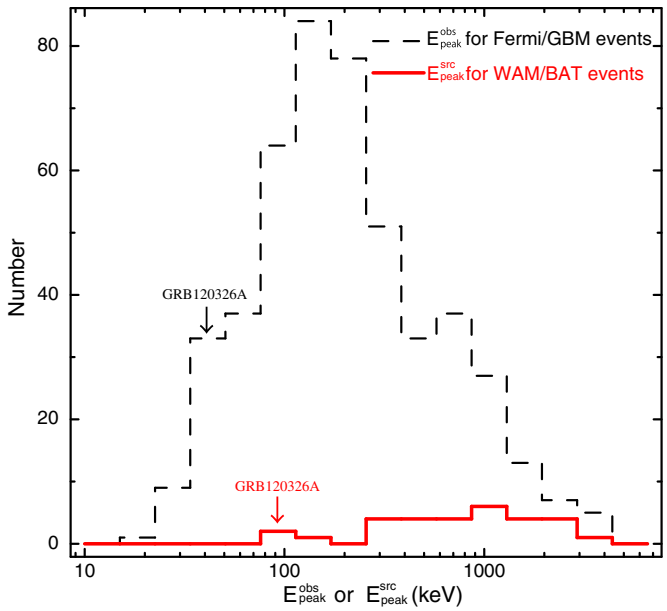

Figure 6. Distribution of $E_{\rm peak}^{\rm src}$ for BAT/WAM events and $E_{\rm peak}^{\rm obs}$ for *Fermi*/GBM events. GRB 120326A is one of the lowest $E_{\rm peak}^{\rm src}$ events among the BAT/WAM sample. $E_{\rm peak}^{\rm obs}$ also shows the same trend with large *Fermi*/GBM samples; though the measurements were analyzed without redshift correction.
(A color version of this figure is available in the online journal.)

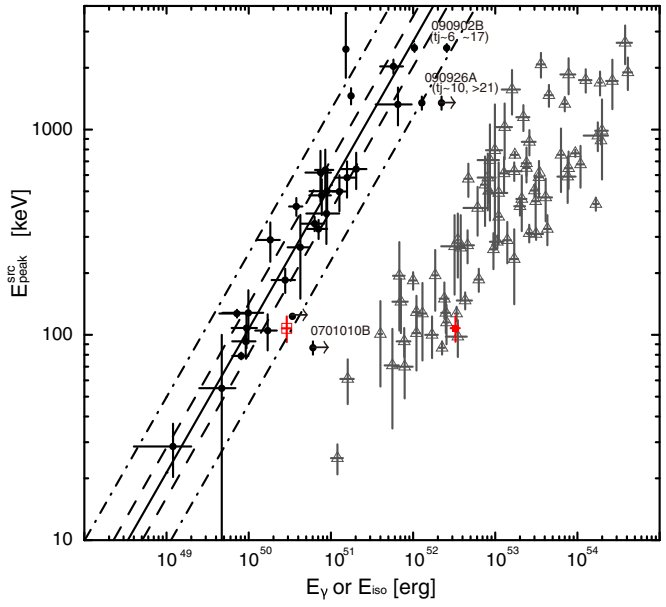

Figure 7. $E_{\rm peak}^{\rm src}$–$E_{\rm iso}$ relation in Amati et al. (2002; open triangle) and the $E_{\rm peak}^{\rm src}$–E_γ relation corrected for a homogeneous circumburst medium (filled circle). GRB 120326A marked with red box points obeyed both relations. The solid line indicates the best-fit correlation derived by Ghirlanda et al. (2007). The dashed and dashed-dotted lines indicate the 1σ and 3σ scatter of the correlation, respectively.
(A color version of this figure is available in the online journal.)

Mészáros 2004) indicates that, of all the $p > 2$ options, the optical results are consistent with both the fast and the slow cooling and both the wind and the ISM medium, as long as $\nu_{m,\rm FS}$ and $\nu_{c,\rm FS}$ lie below the optical band. Here, $\nu_{m,\rm FS}$ and $\nu_{c,\rm FS}$ are the characteristic synchrotron frequency and the cooling frequency based on the standard forward shock synchrotron model. Thus, the jet opening angle and the jet corrected energy are estimated using t_{br} as $6.^\circ 69 \pm 0.^\circ 16$ and $(2.17 \pm 0.10) \times 10^{50}$ erg by assuming the circumburst density, $n = 1.0\ {\rm cm}^{-3}$, and the energy conversion efficiency, $\eta_\gamma = 0.2$. To covert the measured jet break time, t_{br}, to the jet opening angle, we used the formulation of Sari et al. (1999) and Frail et al. (2001). As shown in Figure 7, GRB 120326A obeys the $E_{\rm peak}^{\rm src}$–$E_{\rm iso}$ and $E_{\rm peak}^{\rm src}$–E_γ relations within a 3σ confidence level. Therefore, GRB 120326A belongs to the typical long duration GRB family, even with a low $E_{\rm peak}^{\rm src}$.

4.2. Does the Classical Forward Shock Synchrotron Model Work?

Based on the closure relations, the observed temporal evolution and spectral features of the optical afterglow are consistent with those of the forward shock synchrotron model. The fact that $\nu_{m,\rm FS}$ and $\nu_{c,\rm FS}$ both lie below the optical band implies that within the standard synchrotron model, X-ray afterglows lie in the same spectral regime as the optical emission, and that the standard model predicts the same temporal and spectral shape for X-rays as for the optical.

However, the observed X-ray light curve shows a significant deviation from the predicted behavior of the standard model and appears to require an additional component. Using the testing method of the forward shock model and the decay index (αo–α_X) relation between the optical and X-ray (Urata et al. 2007), we find that GRB 120326A is a clear outlier ($\alpha{\rm o} - \alpha_X = -1.45 \pm 0.10$) and the origin of the X-ray afterglow could differ from that of the optical. For conducting a more rigorous analysis, we selected the normal optical decay phase as from 3.2×10^4 s to 2.1×10^5 s. The optical light curve in this phase is well-fitted with a simple power-law function with an index of -0.96 ± 0.01. For the time range, we forced the X-ray light curve to fit with the simple power-law function and obtained the decay index of -1.54 ± 0.14. Hence, this event remained an outlier ($\alpha{\rm o} - \alpha_X = -0.58 \pm 0.14$) and the X-ray emission could have an extra component such as X-ray flare on the forward shock synchrotron emission.

To check the excess in the X-ray light curve, we shifted the optical light curve to the X-ray band with the factor $(\nu_X/\nu_{\rm opt})^{-p/2}$ by assuming that the X-ray and optical lie on the same segment of the synchrotron radiation. We used $p = 2.48$ with a 3σ error of 0.15 estimated from the optical observations and the closure relation. As shown in Figure 4, the shifted light curve shows a significant gap with that of the observed X-ray and the gap is smaller after $\sim 3 \times 10^5$ s. One of the main reasons for the gap is no consideration of the intrinsic extinction for the optical component at the burst site, which is due to the lack of spectral coverage in the optical observations. If the main X-ray component after 3×10^5 originated from the same segment of forward shock synchrotron radiation with the optical (sharing a similar decay index with that of the optical), $A_V = 0.3 \sim 0.5$ mag with the Small Magellanic Cloud extinction curve is required to fill up the smaller gap after 3×10^5 s. The extinction value of $A_V = 0.3 \sim 0.5$ mag is larger compared to the majority of optically bright events ($A_V < 0.25$ mag; Kann et al. 2006, 2010). We also added the shifted optical light curve with $p = 2$ that provides the upper limit of the forward shock synchrotron radiation under the $p > 2$ condition (Figure 4). Although these imply that adjusting p and introducing extinction may be the solution to explain the gap after 3×10^5, there remains a significant X-ray excess between 2×10^4 and 3×10^5 s.

The forward shock synchrotron model based on the optical afterglow is also unable to explain the submillimeter emission.

Based on the closure relation, the slow decay observed in the submillimeter light curve requires $\nu_{c,\rm FS} < \nu_{\rm submillimeter} < \nu_{m,\rm FS}$ (i.e., a fast cooling condition for both ISM and wind types). Hence, $\nu_{c,\rm FS} < \nu_{\rm submillimeter} < \nu_{m,\rm FS} < \nu_{\rm opt}$ is required to satisfy the closure relation for the submillimeter and optical afterglows altogether. In addition to the closure relation, the observed flux densities (both in the submillimeter and optical bands) at 6.42×10^4 s and the temporal decay index in the optical bands tightly constrain the range of characterized frequencies as $\nu_{c,\rm FS} < 2.3\times10^{11}$ Hz and $\nu_{m,\rm FS} \sim 3\times10^{14}$ Hz in order to make the fast cooling condition. With these conditions, we find that even a drastic case (e.g., $\epsilon_B \sim 1$ and $\epsilon_e \sim 1$ with a very high density of $n >$ several $\times10^3$ cm^{-3}) cannot meet the condition, and that the origin of submillimeter component could also differ from that of the optical. Thus, additional radiation is required to explain X-ray and submillimeter emissions altogether.

4.3. Forward Shock Synchrotron Modeling

To describe the entire spectral energy distribution (SED), we performed modeling for the optical light curves and spectra by using the boxfit code (van Eerten et al. 2012) that involved two-dimensional relativistic hydrodynamical jet simulations to determine the burst explosion and the synchrotron radiation parameters with a homogeneous circumburst medium. Hence, hereafter, we only consider the ISM condition and do not verify whether the ISM or wind condition is favorable. This code also performs data fitting with the downhill simplex method combined with simulated annealing. Based on the observational results, we fixed $\theta_{\rm jet} = 6.^\circ7$ and a power-law electron spectrum of slope $p = 2.5$. The observing angle was also fixed as $\theta_{\rm obs} = 0$. By using only the optical data with the code, we determined the optimal modeling parameters to describe the optical light curves as $E = 3.9\times10^{52}$ erg, $n = 1.0$ cm^{-3}, $\epsilon_B = 1.0\times10^{-3}$, and $\epsilon_e = 6.9\times10^{-1}$. To adjust the model function, we also set the jet opening angle as a free parameter and then $\theta_{\rm jet} = 8.^\circ1$ provided favorable agreement ($\chi^2/\nu = 3.9$ for $\nu = 94$) with observing the light curve. The solid line in Figure 4 indicates the best model function for the r'-band light curve, which also agreed well with the analytical model function. This opening angle adjustment is reasonable because $\theta_{\rm jet} = 6.^\circ7$ was estimated by considering the conical jet. An additional note is that the post-jet-break closure relation is no longer valid under the consideration of the detailed spreading of the jet (van Eerten & MacFadyen 2013). However, we are not concerned about this, since we were able to achieve the good fit with the simulation-based fit models. With the adjusted jet opening angle, GRB 120326A still obeyed the $E^{\rm src}_{\rm peak}$–E_γ relation. We also attempted to determine the optimal solution by using optical and submillimeter data with the code. However, no sufficient solution describes the temporal evolutions of submillimeter and optical afterglows at once, which were determined by the χ^2 evaluation with 2.3×10^4. All of the trials provided reduced χ^2 greater than 13. This is consistent with the forward shock tests described above. We generated the forward shock synchrotron model spectrum by using the boxfit with the best modeling parameters for the light curve. Figure 5 shows the SED at 6.42×10^4 s after the burst. The spectrum in the X-ray and submillimeter exhibited substantial excesses from the best model function and indicated that the afterglow spectrum required additional radiation components. This interpretation is also consistent with the result of the αo–α_X relation and the shifted optical light curve to the X-ray band with factor $(\nu_X/\nu_{\rm opt})^{-p/2}$.

4.4. Reverse Shock and Synchrotron Self-Compton Radiation

A solution that explains the X-ray excess and the different origin of the submillimeter emission is the introduction of synchrotron self-inverse Compton radiation from reverse shock. This is one of the most feasible methods of dealing with two notable observed properties at once. Assuming that the deceleration time is near the X-ray light curve peak at $t_{bX} \sim 5.2\times10^4$ s, the initial Lorentz factor Γ_0 is estimated as $\sim$16, which is consistent with the thin-shell case ($\Gamma_c \sim 365$). Here, Γ_c is the critical Lorentz factor that distinguishes thin shell models, where the reverse shock remains Newtonian, from thick shell models (Sari & Piran 1995; Kobayashi et al. 2007). This lower Γ_0 might be associated with the low $E^{\rm src}_{\rm peak}$ property. It might also originate from the cocoon fireball as part of two-component jet in the collapsar framework (e.g., Ramirez-Ruiz et al. 2002). In this case, thermal radiation is expected to arise in the optical light curves (Kashiyama et al. 2013; Nakauchi et al. 2013). However, the observed optical light curves show no excess in the late phase.

Using the estimated parameters described above, we calculated the model function for synchrotron self-inverse Compton radiation from reverse shock under the thin-shell condition described in Kobayashi et al. (2007). For this calculation, we assumed $\epsilon_{B,\rm RS} \sim 5\times10^{-3}$, and peak flux densities of reverse and forward shocks as $F_{\rm max,RS} \sim 5.5$ mJy and $F_{\rm max,FS} \sim 0.2$ mJy, respectively. Figure 5 shows the calculated spectrum for the reverse shock and inverse Compton components at 6.42×10^4 s with the obtained key parameters of $\nu^{\rm Sync}_{m,\rm RS} \sim 4\times10^{11}$ Hz, $\nu^{\rm Sync}_{c,\rm RS} \sim 7\times10^{12}$ Hz, $\nu^{\rm IC}_{m,\rm RS} \sim 1\times10^{17}$ Hz, and $\nu^{\rm IC}_{c,\rm RS} \sim 4\times10^{19}$ Hz. Although the observed X-ray flux was slightly brighter than the calculated self-inverse Compton component, the total spectrum including forward shock sufficiently described the overall properties of the afterglow. Because $\nu_{\rm obs} < \nu^{\rm Sync}_{m,\rm RS}$, the expected decay index of the reverse shock component in the observed submillimeter band was ~-0.46, which was consistent with the slow temporal evolution of the submillimeter afterglow ($\alpha_{\rm submillimeter} = -0.33$). The evolution, which was relatively shallower than expected, also implies the smooth transition of $\nu^{\rm Sync}_{m,\rm RS}$ in the observing band, unlike the sharp break in Figure 4. This could be consistent with other spectrum breaks such as the non-existence of the sharp cooling break in the afterglow spectrum (e.g., Granot & Sari 2002; van Eerten & Wijers 2009; Curran et al. 2010). The observed X-ray decay ($\alpha_X \sim -2.4$) and spectrum ($\beta_X \sim -0.96$) indices were also basically consistent with the expected values ($\alpha_X \sim -2.8$ and $\beta_X \sim -0.75$) for $\nu^{\rm IC}_{m,\rm RS} < \nu_{\rm obs} < \nu^{\rm IC}_{c,\rm RS}$.

5. SUMMARY

We conducted multi-wavelength observations of a typical long-duration GRB 120326A, including rapid observations using SMA. Our SMA observation successfully made the fastest afterglow detection among seven submillimeter afterglows at 230 GHz and monitored from 4.32×10^4 to 3.46×10^5 s. The submillimeter afterglow showed considerably slower temporal evolution ($\alpha_{\rm submillimeter} = -0.33\pm0.08$) which is not likely to be explained by the forward shock synchrotron model. Based on our dense optical observations, we found that the optical afterglows were well-fitted by the broken power-law model, and the forward shock synchrotron model is feasible to explain the properties. With the boxfit code, we also found the reasonable model function within the forward shock synchrotron model

under the assumption of ISM circumburst medium. Using the simple testing method of the forward shock model with temporal decay indices of optical and X-ray afterglows, we found that the origin of the X-ray afterglow could differ from that of the optical. Our joint spectrum fitting for prompt emission using *Swift*/BAT and *Suzaku*/WAM also characterized the event and found that the current event obeys the $E^{\rm src}_{\rm peak}$–$E_{\rm iso}$ and $E^{\rm src}_{\rm peak}$–E_{γ} relations within a 3σ confidence level.

Based on the detection and the slow decay of the afterglow in submillimeter, we introduced the synchrotron self-inverse Compton radiation from reverse shock and found that this is a plausible method to explain the diversity. This successful modeling could benefit other GRBs. Similar to GRB 120326A, numerous events exhibited no apparent jet breaks in the X-ray band and different temporal evolutions between the X-ray and optical. These observational properties imply that additional components, such as reverse shock and its synchrotron self-inverse Compton radiation, cause different temporal evolution and hide obvious jet breaks in the X-ray. Because of a lack of submillimeter observations for these samples, interpretation from the same picture for these events was difficult. Thus, further rapid follow-ups and continuous monitoring with submillimeter instruments such as SMA and ALMA will enable systematic testing of the reverse shock and self-inverse Compton radiation.

We thank Glen Petitpas for various arrangements on the SMA observations and Shiho Kobayashi for useful comments. We also thank all of staff at the Lulin observatory. This work is partly supported by the Ministry of Education and the National Science Council of Taiwan grants NSC 100-2112-M-008-007-MY3(YU), 99-2112-M-002-002-MY3(KYH). M.I., J.W.K., M.J., and S.J. acknowledge support from the National Research Foundation of Korea (NRF) grant No. 2008-0060544, funded by the Korea government (MSIP). This work made use of data supplied by the UK Swift Science Data Centre at the University of Leicester. This paper includes data taken at the McDonald Observatory of the University of Texas in Austin. The PS1 Surveys have been made possible through contributions of the Institute for Astronomy, the University of Hawaii, the Pan-STARRS Project Office, the Max-Planck Society and its participating institutes, the Max Planck Institute for Astronomy, Heidelberg and the Max Planck Institute for Extraterrestrial Physics, Garching, The Johns Hopkins University, Durham University, the University of Edinburgh, Queen's University Belfast, the Harvard-Smithsonian Center for Astrophysics, and the Las Cumbres Observatory Global Telescope Network, Incorporated, the National Central University of Taiwan, and the National Aeronautics and Space Administration under grant No. NNX08AR22G, issued through the Planetary Science Division of the NASA Science Mission Directorate.

REFERENCES

Akerlof, C., Balsano, R., Barthelmy, S., et al. 1999, Natur, 398, 400
Amati, L., Frontera, F., Tavani, M., et al. 2002, A&A, 390, 81
Berger, E., Sari, R., Frail, D. A., et al. 2000, ApJ, 545, 56
Chandra, P., Cenko, S. B., Frail, D. A., et al. 2008, ApJ, 683, 924
Collazzi, A. C. 2012, GCN, 13145, 1
Curran, P. A., Evans, P. A., de Pasquale, M., Page, M. J., & van der Horst, A. J. 2010, ApJL, 716, L135
de Ugarte Postigo, A., Lundgren, A., Martín, S., et al. 2012, A&A, 538, A44
Evans, P. A., Beardmore, A. P., Page, K. L., et al. 2007, A&A, 469, 379
Evans, P. A., Beardmore, A. P., Page, K. L., et al. 2009, MNRAS, 397, 1177
Frail, D. A., Kulkarni, S. R., Sari, R., et al. 2001, ApJL, 562, L55
Galama, T. J., Bremer, M., Bertoldi, F., et al. 2000, ApJL, 541, L45
Granot, J., & Sari, R. 2002, ApJ, 568, 820
Gehrels, N., Chincarini, G., Giommi, P., et al. 2004, ApJ, 611, 1005
Ghirlanda, G., Nava, L., Ghisellini, G., & Firmani, G. 2007, A&A, 466, 127
Gorosabel, J., de Ugarte Postigo, A., Castro-Tirado, A. J., et al. 2010, A&A, 522, A14
Greiner, J., Krühler, T., McBreen, S., et al. 2009, ApJ, 693, 1912
Han, W., Mack, P., Lee, C.-U., et al. 2005, PASJ, 57, 821
Ho, P. T. P., Moran, J. M., & Lo, K. Y. 2004, ApJL, 616, L1
Huang, K. Y., Urata, Y., Filippenko, A. V., et al. 2005, ApJL, 628, L93
Huang, K. Y., Urata, Y., Kuo, P. H., et al. 2007, ApJL, 654, L25
Iwakiri, W., Tashiro, M., Terada, Y., et al. 2012, GCN, 13176, 1
Laskar, T., Zauderer, A., & Berger, E. 2012, GCN, 13181, 1
Lee, I., Im, M., & Urata, Y. 2010, JKAS, 43, 95
Li, L., Liang, E.-W., Tang, Q.-W., et al. 2012, ApJ, 758, 27
Lim, J., Chang, S., Pak, S., et al. 2013, JKAS, 46, 161
Kann, D. A., Klose, S., & Zeh, A. 2006, ApJ, 641, 993
Kann, D. A., Klose, S., Zhang, B., et al. 2010, ApJ, 720, 1513
Kashiyama, K., Nakauchi, D., Suwa, Y., Yajima, H., & Nakamura, T. 2013, ApJ, 770, 8
Kim, E., Park, W.-K., Jeong, H., et al. 2011, JKAS, 44, 115
Klotz, A., Gendre, B., Boer, M., & Atteia, J. L. 2012, GCN, 13107, 1
Kobayashi, S., Zhang, B., Mészáros, P., & Burrows, D. 2007, ApJ, 655, 391
Kulkarni, S. R., Frail, D. A., Sari, R., et al. 1999, ApJL, 522, L97
Magnier, E. A., Schlafly, E., Finkbeiner, D., et al. 2013, ApJS, 205, 20
Meszaros, P., & Rees, M. J. 1997, ApJ, 476, 232
Mitsuda, K., Bautz, M., Inoue, H., et al. 2007, PASJ, 59, 1
Nakauchi, D., Kashiyama, K., Suwa, Y., & Nakamura, T. 2013, ApJ, 778, 67
Ohno, M., Fukazawa, Y., Takahashi, T., et al. 2008, PASJ, 60, 361
Panaitescu, A., Mészáros, P., Burrows, D., et al. 2006, MNRAS, 369, 2059
Panaitescu, A., & Vestrand, W. T. 2011, MNRAS, 414, 3537
Park, W.-K., Pak, S., Im, M., et al. 2012, PASP, 124, 839
Perley, D. A., Alatalo, K., & Horesh, A. 2012, GCN, 13175, 1
Ramirez-Ruiz, E., Celotti, A., & Rees, M. J. 2002, MNRAS, 337, 1349
Resmi, L., Ishwara-Chandra, C. H., Castro-Tirado, A. J., et al. 2005, A&A, 440, 477
Sakamoto, T., Hullinger, D., Sato, G., et al. 2008, ApJ, 679, 570
Sakamoto, T., Lamb, D. Q., Kawai, N., et al. 2005, ApJ, 629, 311
Sari, R., & Piran, T. 1995, ApJL, 455, L143
Sari, R., Piran, T., & Halpern, J. P. 1999, ApJL, 519, L17
Schlafly, E. F., & Finkbeiner, D. P. 2011, ApJ, 737, 103
Schlafly, E. F., Finkbeiner, D. P., Jurić, M., et al. 2012, ApJ, 756, 158
Sheth, K., Frail, D. A., White, S., et al. 2003, ApJL, 595, L33
Siegel, M. H., Barthelmy, S. D., Burrows, D. N., et al. 2012, GCN, 13105, 1
Sugita, S., Yamaoka, K., Ohno, M., et al. 2009, PASJ, 61, 521
Takahashi, T., Abe, K., Endo, M., et al. 2007, PASJ, 59, 35
Tashiro, M. S., Abe, K., Angelini, L., et al. 2007, PASJ, 59, 361
Tello, J. C., Sanchez-Ramirez, R., Gorosabel, J., et al. 2012, GCN, 13118, 1
Toma, K., Ioka, K., & Nakamura, T. 2008, ApJL, 673, L123
Tonry, J. L., Stubbs, C. W., Lykke, K. R., et al. 2012, ApJ, 750, 99
Urata, Y., Huang, K., Im, M., et al. 2009, ApJL, 706, L183
Urata, Y., Huang, K. Y., Takahashi, S., & Petitpas, G. 2012, GCN, 13136, 1
Urata, Y., Nishiura, S., Miyata, T., et al. 2003, ApJL, 595, L21
Urata, Y., Yamazaki, R., Sakamoto, T., et al. 2007, ApJL, 668, L95
van Eerten, H., & MacFadyen, A. 2013, ApJ, 767, 141
van Eerten, H., van der Horst, A., & MacFadyen, A. 2012, ApJ, 749, 44
van Eerten, H. J., & Wijers, R. A. M. J. 2009, MNRAS, 394, 2164
von Kienlin, A., Meegan, C. A., Paciesas, W. S., et al. 2014, ApJS, 211, 13
Walker, C., Court, J., Duffy, R., et al. 2012, GCN, 13112, 1
Yamaoka, K., Endo, A., Enoto, T., et al. 2009, PASJ, 61, S35
Zhang, B., & Mészáros, P. 2004, IJMPA, 19, 2385